Growth from Below: Graphene Bilayers on Ir(111)

Shu Nie,[†] Andrew L. Walter,[‡,§] Norman C. Bartelt,[†] Elena Starodub,[†] Aaron Bostwick,[‡] Eli Rotenberg,[‡] and Kevin F. McCarty[†,*]

[†]Sandia National Laboratories, Livermore, California 94550, United States, [‡]Advanced Light Source, E.O. Lawrence Berkeley National Laboratory, Berkeley, California 94720, United States, and [§]Department of Molecular Physics, Fritz-Haber-Institut der Max-Planck-Gesellschaft, 14195 Berlin, Germany

ABSTRACT We elucidate how graphene bilayers form on Ir(111). Low-energy electron diffraction (LEED) reveals that the two graphene layers are not always rotationally aligned. Monitoring this misalignment during growth shows that second-layer islands nucleate between the existing layer and the substrate. This mechanism occurs both when C segregates from the Ir and when elemental C is deposited from above. Low-energy electron microscopy (LEEM) and angle-resolved photoemission spectroscopy (ARPES) show that second-layer nucleation occurs preferentially under the first-layer rotational variants that are more weakly bound to the substrate. New-layer nucleation tends to occur inhomogeneously at substrate defects. Thus new-layer nucleation should be rapid on substrates that weakly bind graphene, making growth unstable toward mound formation initiated at substrate defects. In contrast, stronger binding permits layer-by-layer growth, as for Ru(0001). ARPES shows that bilayer graphene has two slightly p-doped π-bands. The work function of bilayer graphene is dominated by the orientation of the bottom layer.

KEYWORDS: bilayer graphene · Ir(111) · Ru(0001) · low-energy electron microscopy · low-energy electron diffraction · angle-resolved photoemission spectroscopy · work function

Much effort has been recently devoted to growing large defect-free graphene sheets.[1] Obtaining either single layers or bilayers of uniform thickness is desirable for many purposes.[2−4] Controlling the relative stacking of multilayer graphene is also important since stacking alters electronic properties.[5−8] One route to making such films is growth on metals.[9−15] There is a reasonable understanding of how single-layer graphene forms on metals.[15−17] On transition metals such as Ru and Ir, the first layer grows by supersaturation of a carbon adatom gas.[18−20] This growth mechanism is independent of the C source and depends only on the adatom concentration. Islands typically nucleate at defects on the metal surface.

Synthesizing uniform defect-free multilayers is more difficult, and the growth mechanisms are understood less. Growing multilayers requires a source of C at slightly higher chemical potential (larger carbon concentration) than does the first layer.[11] Chemical vapor deposition (CVD) is the most common growth method on metals.[15] However, the rate of hydrocarbon decomposition in CVD slows greatly once the catalytic metal is completely covered by a single graphene layer.[19] Achieving the C adatom supersaturations needed to nucleate and grow multilayers is then difficult. In contrast, multilayers readily grow if C segregates from the substrate[11] or if elemental C is directly deposited, as discussed here. Since significant amounts of C can dissolve into many metals at CVD temperatures,[21] understanding segregation has long been recognized as being important.[11] In fact, this bulk C can segregate and form multilayers during cooling after the CVD process ends.[16] Such segregation makes single-layer synthesis difficult on metals like Ni[22] in which C is highly soluble. Unwanted multilayer growth by segregation can be avoided using metals with very low C solubility, such as Cu,[23] and a vapor source of C. However, graphene growth from segregation can occur even for metals with relatively low bulk solubility, like Ir[24] and Ru.[25]

This paper's goal is determining how graphene sheets are added to a metal already covered by one layer. The first question we address is whether additional layers nucleate from above, as in Figure 1a, or from below, as in Figure 1b. Naively one might expect that C diffusion through the existing graphene sheet is difficult, so that segregation would lead to growth from below. Similarly, deposition from above would lead to growth from above. Tontegode and coworkers provided evidence from Auger electron spectroscopy that a second layer grows under first-layer graphene during segregation on Re and during C deposition on Ir(111).[26,27] On the basis of scanning tunneling microscopy (STM) images from bilayers on Ru(0001), Cui, Fu and Bao

*Address correspondence to mccarty@sandia.gov.

Received for review December 23, 2010 and accepted January 28, 2011.

Published online February 15, 2011
10.1021/nn103582g

proposed that growth by segregation occurred from below.[28] However, the generality of this mechanism and its implications for the quality of graphene bilayers are unclear.

We use low-energy electron microscopy (LEEM) to observe bilayer growth on Ir(111). The system is apt for studying bilayer formation because several rotational domains of graphene that differ in in-plane orientation can coexist.[24] By monitoring rotational misalignments between the first and second layers, we unambiguously deduce that the second layer grows underneath the first layer. This "underlayer" mechanism (Figure 1b) occurs both when the C is coming from below by segregation and from above by C deposition. These observations suggest that multilayer growth observed on Ni during CVD might also occur from below.[22,29] Because adding new layers requires existing layers to debond, different factors control the film quality compared to conventional growth. For example, using LEEM and angle-resolved photoemission spectroscopy (ARPES), we find large spatial variations in second-layer nucleation rates that are correlated with the energy needed to debond the first layer. Nucleation is sufficiently rapid at certain points on the surface that new layers start before the existing layers are completed. Thus, on metals that weakly bind graphene, growth is unstable toward making mounds rather than uniform multilayers. ARPES also shows that bilayer graphene has two slightly p-doped π-bands. Finally, we discuss how the relative orientations of graphene bilayers influence work function.

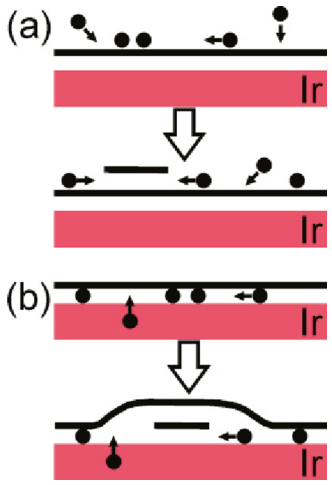

Figure 1. Two scenarios for growth of the second graphene layer on metal substrates. (a) Second layer grows on top of the first layer. (b) Second layer grows between the first layer and the substrate.

RESULTS AND DISCUSSION

New Layers Grow Underneath Existing Layers during Surface Segregation. Figure 2 shows LEEM images as graphene grows on Ir(111) by surface segregation (see Methods for experimental details). At 1130 °C, monolayer graphene nucleates and grows to cover the surface (Figure 2a). During subsequent cooling, a second graphene layer nucleates (Figure 2b), as determined from the LEEM intensity variation with electron energy (see Figure S1 of the Supporting Information). Unlike graphene grown on Ru(0001), many rotational variants of single-layer graphene occur on Ir(111). Their growth and structure have been characterized using LEEM, low-energy electron diffraction (LEED), STM, and ARPES.[19,24,30] Figure 2a contains an example of two rotational variants labeled as R0/Ir and R22/Ir, which have different contrast in LEEM. In the R0 variant, the graphene and Ir lattices are aligned; that is, the [11$\bar{2}$0] direction of the single-layer graphene lies along the Ir [110] direction. In R22, the graphene lattice is rotated 22° from the R0 orientation.

The domain structure in the first layer allows us to discriminate between second-layer growth from above or below. If the second layer grows underneath, the domain structure of the first layer is preserved as it debonds from the substrate to become the uppermost layer (Figure 1b). However, the domain structure of the top layer could differ from the first-formed layer if the second layer nucleates on top (Figure 1a). Which layer is uppermost can be determined by the relative intensity of diffraction features. The differences in LEED can be observed where second-layer islands grow across rotational boundaries in the first layer. When crossing these boundaries, we do not expect the top

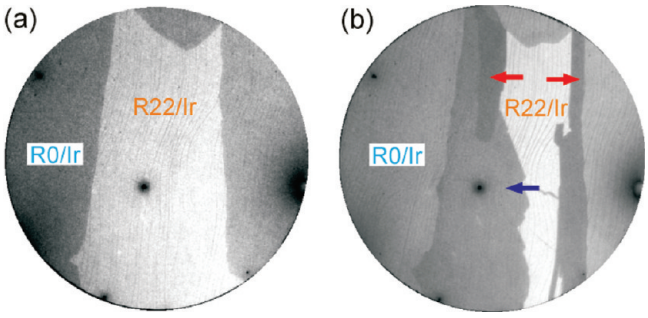

Figure 2. Single- and bilayer graphene on Ir(111) grown from segregating carbon. (a) LEEM image of R0 and R22 domains of single-layer graphene at 1130 °C. (b) After cooling to room temperature. The R22 region now has bilayer graphene islands with two contrasts, as indicated by red and blue arrows. Field of view is 20 μm.

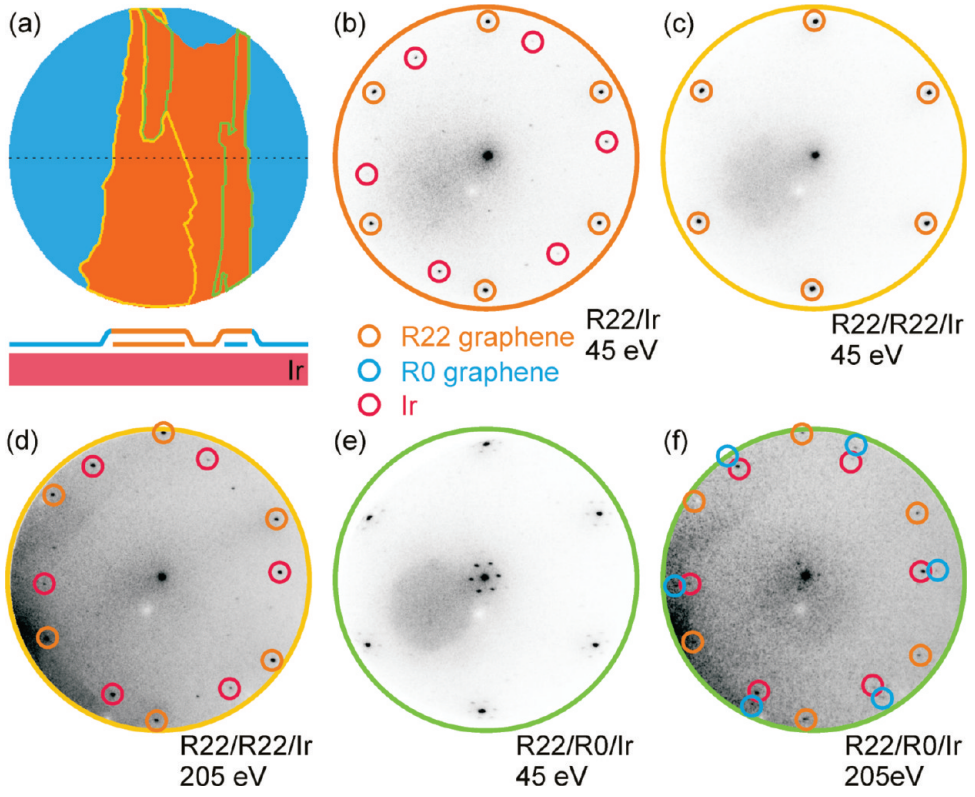

Figure 3. Underlayer growth mechanism during segregation. (a) Upper panel is a color-coded image of Figure 2b. The bilayer graphene islands in the R22 domain are outlined. Lower panel is a cross section of the graphene topography along the black dashed line. (b) LEED at 45 eV from the bright single-layer R22/Ir area in Figure 2b. (c,d) LEED at 45 and 205 eV from the bilayer area outlined in yellow. Both graphene layers are rotated 22° relative to Ir, as shown in the cross section. (e,f) LEED at 45 and 205 eV from the bilayer area outlined in green. One graphene layer is rotated 22° relative to Ir; the other is aligned with Ir. Diffraction at 45 eV is dominated by the 22°-rotated graphene, showing that the rotated layer is on the top.

graphene sheet to rotate to match the new orientation of the underlying sheet—such rotations require creating new high-energy defects in the growing graphene. Indeed, Sutter and co-workers showed that graphene sheets preserve their in-plane orientations when growing across boundaries between Ru grains with different in-plane orientation.[31] In the following, we identify the uppermost layer with diffraction and show that the original domain structure is preserved in the top layer, providing concrete evidence that the second layer grows under the first.

Figure 2b shows that the second-layer islands grown in the R22/Ir area during cooling to 1080 °C have two different contrasts. These two domains are outlined in yellow and green, respectively, in Figure 3a. We next show that the bilayer contrasts correspond to different orientations of the second layer, analogous to the contrast between rotational variants of first-layer graphene. In Figure 3b–f, selective-area LEED is used to identify the orientation of the first and second graphene layers.[24] Blue and orange show the R0/Ir and R22/Ir first-layer domains, respectively. The areas inside the yellow and green lines in Figure 3a are where the second layer formed. Figure 3b shows LEED from the single-layer R22/Ir region. The first-order (0,1) diffraction spots from the R22 graphene and the Ir are circled in orange and red, respectively. Figure 3c shows LEED from the bilayer region outlined in yellow in Figure 3a at the same low electron energy (45 eV). The R22 graphene (0,1) spots, circled orange in Figure 3c, are stronger than those in Figure 3b. The Ir (0,1) spots and the double-diffraction spots from the graphene and Ir lattices have disappeared. At the much higher electron energy (205 eV) of Figure 3d, diffraction from Ir (red circles) is much stronger, consistent with the greater electron penetration and escape depths.[32] At electron energies between 30 and 500 eV, all observed diffraction spots are assignable to R22 graphene on the Ir substrate. Thus, we identify the yellow-circled region in Figure 3a as two stacked R22 layers, which we denote as R22/R22/Ir. At this stage, because the two layers have the same orientation, we cannot tell by diffraction whether the second layer formed under or on top of the initial R22 layer.

This is not the case for the bilayer regions outlined in green in Figure 3a. This region's diffraction pattern at 45 eV (Figure 3e) has pronounced first-order spots from R22 graphene, showing that the upper sheet has R22 orientation. Higher energy (Figure 3f) reveals diffraction from R0 graphene (blue circles) and the Ir (red circles). The diffraction from R22 at low energy and from R0 at high energy provides persuasive evidence

that R0 graphene is below the R22 graphene.[33] Since we know that the R22 layer formed first (Figure 2a), we conclude that the second layer nucleated under the first layer, giving a R22/R0/Ir stacking. The schematic cross section in Figure 3a illustrates, along the dashed line in the LEEM image, the topography and the two types of second-layer islands that nucleated under the original R22 sheet.

Additional details in the diffraction patterns are consistent with our assignment of the layer stacking. Figure 3e has pronounced sets of 6-fold spots around the specular beam (center) and the (0,1) graphene spots of R22/Ir. The orientation and spacing of these "rosettes" are the same as observed in single-layer R0/Ir (see Figure S1c in Supporting Information). They are characteristic of the periodicity of the moiré formed by the R0 graphene lattice next to the Ir lattice.[34] An additional example of rosettes from a bilayer with R0 next to Ir is shown in Figure S2.[35] Thus, all of the diffraction features support the conclusion that graphene with two orientations grew under a top sheet.

Second-Layer Growth Occurs Underneath Even during Deposition of Elemental Carbon. We now show that the second layer grows underneath the first layer even when depositing C from above. The evidence comes from observing how second layers grow across rotational boundaries in complete first-layer sheets. Figure 4a shows the starting configuration after segregation has stopped. The boundary between two types of first-layer graphene, R0/Ir and R26/Ir, is highlighted by the red dotted line. Some second-layer islands (bright features) exist in the R26/Ir region. Figure 4b shows the evolution after 44 min exposure to a source of elemental carbon. As established by LEED, most of the R26/Ir region is now covered by a second layer of R26 orientation, giving a local R26/R26/Ir stacking. After deposition, the original R0/Ir region has a finger-shaped lobe, which lies along the dashed line in Figure 4b. Inspection of movie S1 (Supporting Information) shows that the lobe formed when the second layer filled the R26/Ir region and then grew across the rotational boundary and into the R0/Ir region.

The lobe is outlined in orange in the higher-resolution, room-temperature image of Figure 4c. Its second layer should have R26 orientation since it must be an extension of one layer of the R26/R26/Ir configuration from which it grew. The LEED pattern of the lobe in Figure 4d shows in three ways that the topmost layer is R0 graphene and the bottom layer is R26 (i.e., R0/R26/Ir). First, the most intense graphene spots are aligned with Ir, as seen by comparing their orientation with the red-circled Ir spots in Figure 3b. Second, the first-order spots associated with R26 are barely visible. Third, the presence of the double-diffraction spots from the R26 and Ir lattices shows that R26 is next to Ir.[35] The schematics under Figure 4a,b give the cross sections

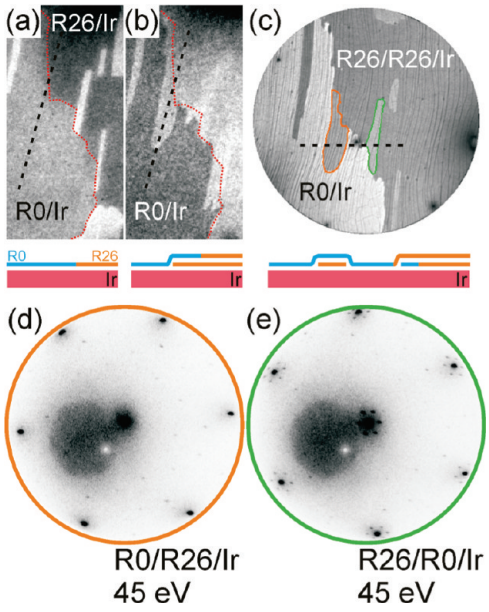

Figure 4. Underlayer growth mechanism during C deposition. (a,b) Upper panels are LEEM images (9.7 μm $\times$ 19.5 μm) before and after depositing elemental C at 790 °C. Red dotted line is the boundary between R26 and R0 domains of first-layer graphene. Bright areas are bilayer islands. Lower panels show the cross sections along the black dashed lines before and after growth. (c) Same area at room temperature after growth. The bilayer region inside the orange line was created by a second layer growing from the R26 region across the rotational boundary and into the R0 region. The area inside the green line is a bilayer domain that slowly expanded from a bilayer island present in the R26 domain before C deposition. Field of view = 20 μm. (d) LEED pattern from the orange area showing that its topmost layer is R0 graphene. (e) LEED pattern from the green area showing that its topmost layer is R26 graphene.

along the black dashed lines, showing how the R26 layer grew under the first layer and across the R26/R0 rotational boundary.

Our interpretation of the diffraction is reinforced by analyzing the area outlined in green in Figure 4c. This region grew from one of the bright second-layer islands under R26/Ir in Figure 4a. In contrast to the strong R0 diffraction in Figure 4d, diffraction from this region (Figure 4e) shows strong R26 graphene spots surrounded by 6-fold rosettes. Again, the latter arise from R0 next to Ir. Thus, the green-circled region has R26/R0/Ir configuration, as shown in the cross section of Figure 4c. This region grew slower than the adjacent R26/R26/Ir region.[36]

These observations strongly suggest that the second-layer graphene grows between the first graphene layer and Ir (Figure 1b), independent of whether the C is coming from below by segregation (Figure 3) or from above by deposition (Figure 4), as suggested by Tontegode *et al.*[27] We next discuss the consequences of this atypical mechanism.

Implications of the Underlayer Growth Mechanism. Since film growth typically occurs by nucleation on top (Figure 1a),[37] the underlayer mechanism of graphene

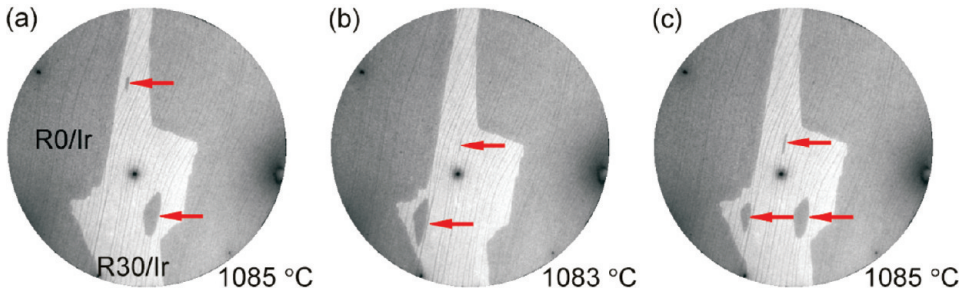

Figure 5. LEEM images after cooling three sequential times from ~1100 °C. The second-layer islands, marked by red arrows, nucleated at the same locations within an R30/Ir domain. No second layers formed in the surrounding R0/Ir domain within the field of view (20 μm).

growth has unusual features. Inserting a new layer next to the substrate requires debonding the existing graphene from the substrate. We see direct consequences of this debonding and nucleation next to the substrate. Using LEEM, we find that the nucleation density of second-layer islands is not uniform over the surface. Instead, it strongly depends on the alignment of the first layer with respect to the Ir. Figure 2b provides an example where no second-layer islands nucleated under R0 during segregation. Instead, all of the nucleation occurred under rotated first-layer graphene (R22). During C deposition, Figure S4 shows second-layer nucleation under rotated R30 but not under R0 graphene. Surveying several square millimeters of area in different films confirms a strong preference for the second layer to nucleate under rotated (non-R0) first-layer domains. Furthermore, Figure 5 and its movie version (movie S3, Supporting Information) show second-layer nucleation during repeated cycles between ~1080 °C, where second layer nucleates, and ~1110 °C, where it dissolves. Two to three second-layer islands nucleate under ~120 μm^2 of R30 graphene. No islands nucleate under ~200 μm^2 of R0 graphene. In addition, ARPES (see next section) shows two π-bands for rotated variants but not for R0, consistent with there being second-layer graphene under rotated first layer but not under R0 first layer.

In principle, a number of factors could control how new layers nucleate under existing layers, including differences in C diffusion under different rotational domains and, as discussed below, the domain size. However, an ARPES/Raman spectroscopy study has established that the R0 variant interacts more strongly with the Ir than a rotated (R30) variant.[30] Thus, we suggest that the rarity of nucleation under R0 graphene is a consequence of the relative difficulty of debonding this orientation from the Ir.

In the underlayer mechanism, the substrate plays a much larger role in new-layer nucleation than in conventional film growth. Figure 5 and movie S3 show that second-layer islands nucleate at the same sites in the interior of a single rotated R30/Ir domain. This preference for nucleation within first-layer domains suggests that new layers originate at defects on the Ir surface rather than at domain boundaries or other defects in the first graphene layer. The substrate's effect is also seen in the orientation of the second layer. On the basis of six different films each surveyed over millimeter distances, we find that the second layer has only two orientations—that of the substrate or that of the first layer.[38] (In contrast, the first layer has at least six orientations.) While the second-layer orientation depends on the orientations of both the substrate and the first layer, the fact that it depends at all on the substrate is a unique consequence of the underlayer mechanism.

The substrate's influence is also seen in the shapes of the second-layer islands. As Figures 2b and 4c show, the islands are markedly elongated along the direction of the Ir steps, which run roughly vertically in the images. The same elongation along steps occurs in the first-layer islands[19] and is a natural result of the second layer growing next to the substrate. While the substrate steps dominate the shape of the second-layer islands, the relative orientation of the two graphene layers also has a subtle effect: second-layer islands aligned with the Ir have higher aspect ratios, while rotated islands have lower aspect ratios. Aligned islands also grow slower than rotated islands. During heating, rotated second-layer islands (such as R22/R22/Ir) dissolve first. Thus, rotated (non-R0) bottom-layer graphene islands are less stable than R0 (nonrotated) islands.

We occasionally find second graphene layers under R0 even though it is the most strongly bound variant.[30] R0 is also the most abundant variant, and its domains can be very large. In such domains, not all C atoms segregating from Ir can diffuse far enough to reach the more loosely bound rotated domains. Supporting Information Figure S1 shows that the second and third layers under R0 have R0/R0/Ir and R0/R0/R0/Ir stacking, respectively. Again, the islands are elongated along the Ir steps, growth shapes that result from the underlayer mechanism. We note that second-layer islands on Ru(0001) are also aligned preferentially along substrates steps.[16] In fact, Figure S5 and movie S4 (Supporting Information) show that Ru steps influence second- and third-layer growth at least as much as the

first layer. These observations suggest that the same underlayer mechanism (Figure 1b) occurs in the Ru system as reported in ref 28. Indeed, we speculate that growth from below is important for many metal substrates.

Debonding driven by segregation is possible because the graphene−metal interaction is relatively weak (typically less than ∼100 meV/C[39]) compared to typical C segregation energies (a few tenths eV/C[11] to several eV/C[20]). However, our C deposition experiments (Figure 4 and Figure S4) reveal that C atoms on top of the graphene have a remarkable ability to penetrate a complete single-layer film and ultimately lead to debonding. Our observations do not provide insight, however, into where the carbon atoms go through the first layer to form the second layer. The rotational boundaries and other defects of the first layer might provide a pathway. We note that C adatoms bind almost as strongly to Ir and Ru as C is bound in graphene.[19] Since C adatoms on top of graphene are weakly bound, there is a strong energetic driving force for these C adatoms to go underneath, either into 3-fold hollow sites of these substrates or into their bulk. Hence, a route to minimizing multilayer formation may be using substrates that weakly bind C adatoms, like Cu.[40] Removing the driving force for adatoms to go to the substrate would slow permeation even if the substrate weakly binds graphene. Perhaps this is another reason besides low solubility[23] that aids single-layer formation on Cu.

We end this section by discussing how the underlayer mechanism affects the uniformity of multilayers. Again, the key point is that debonding is required to nucleate new layers even at defects such as bunches of substrate steps. The debonding energy then critically controls the rate at which new layers nucleate. If the energy is sufficiently low, new layers will repeatedly nucleate at substrate defects before prior layers expand to give uniform coverage. Figure S1 shows an example of third-layer formation under the most strongly bound variant (R0) while the second layer only covers a fraction of the surface. Thus, metals that weakly bind graphene are unstable toward making multilayer mounds, as shown in the schematic in Figure 6a. Such mounds have been observed on Pt(111)[41] and Pd(111).[42] At the other extreme, in systems with stronger graphene/substrate binding, the underlayer mechanism enhances layer-by-layer growth (Figure 6b). Ru(0001) may be an example, as reported by Cui, FU and Bao.[28] Figure S5 and its movie version (movie S4) provide another example of layer-by-layer growth on Ru(0001).

Electronic Properties of Bilayer Graphene. In this section, we use ARPES to evaluate independently the uniformity of second-layer nucleation and to characterize the electronic band structures of two different stackings of bilayer graphene on Ir. We examined a sample covered

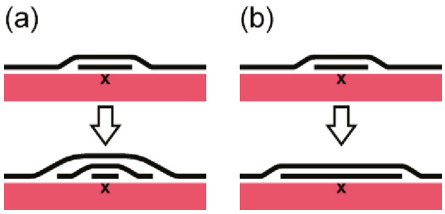

Figure 6. (a) New-layer nucleation occurring repeatedly at a defect (labeled by x) on a metal that weakly binds graphene. Faster nucleation relative to expansion of the older layers leads to nonuniform coverage. (b) Layer-by-layer growth by the underlayer mechanism on a substrate that strongly binds graphene.

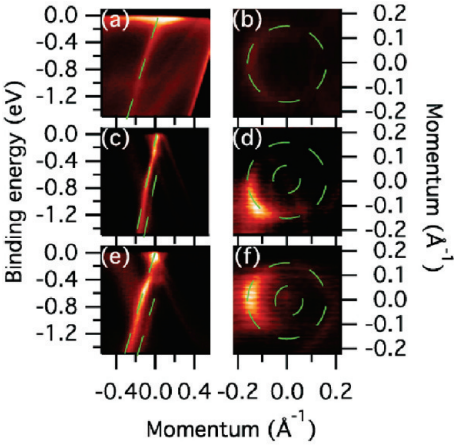

Figure 7. ARPES of a graphene film containing bilayer regions on Ir(111). Top panels: R0/Ir. Middle panels: R22/R22/Ir. Bottom panels: R30/R30/Ir. Left panels: Energy vs momentum along the direction between the Γ point and the K point of the specific graphene variant; the K point is set as the origin. Right panels: Map of states around the graphene K points at a binding energy −0.75 eV below the Fermi level. The Dirac cones are marked with dashes lines.

by one complete graphene layer and roughly 20% of a second layer. The ARPES data are presented in Figure 7 with dashed green lines indicating the graphene bands; all other bands are from the substrate. Analysis around the K point of R0 graphene (Figure 7a) revealed only a single π-band, characteristic of single-layer graphene on Ir.[30] In contrast, Figures 7c,e show the two π-bands characteristic of Bernal-stacked bilayer graphene[6,43] around the K points of R22 and R30 graphene. While ARPES is only able to ascertain the presence of rotationally aligned bilayers, the ARPES analysis is still consistent with the LEEM result that second layer nucleates preferentially under the first-layer sheets rotated from the R0 orientation.[44] In both types of bilayers, R22/R22/Ir and R30/R30/Ir, the π-bands are perturbed relatively little from the bands of free-standing graphene. This result shows that the film/substrate bonding is relatively weak, as also found for single-layer R30 graphene.[30] Figures 7b,d,f map out, in two momentum directions, the constant-energy contours at a binding energy −0.75 eV below Fermi level. The two concentric, circular π-bands from the

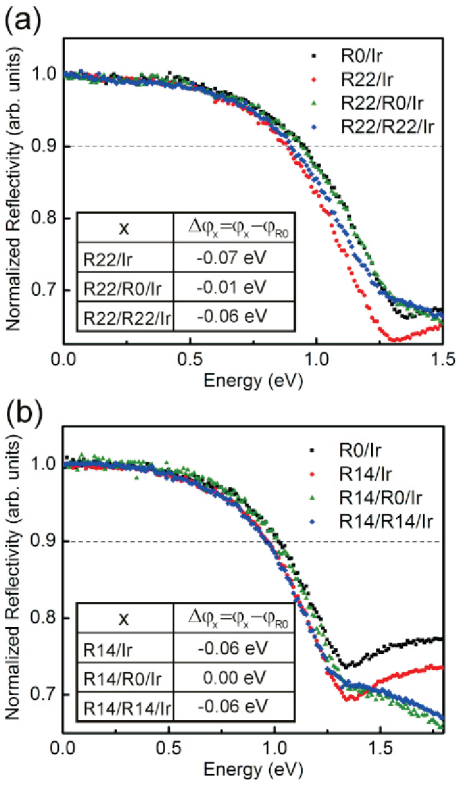

Figure 8. Effect of layer thickness and bilayer orientation on work function of graphene-covered Ir(111). (a) Electron reflectivity vs energy from R0 and R22 single layers and two different bilayer orientations under a top R22 sheet. (b) Electron reflectivity vs energy from R0 and R14 single layers and two different bilayer orientations under a top R14 sheet. Insets show the work function difference between the stacking sequence labeled x and single-layer R0. Bilayer work functions are controlled by the orientation of the layer adjacent to the substrate.

bilayers are again marked by dashed lines. From these maps, we calculate that both types of bilayers are slightly p-doped to a level of $1 \times 10^{11}/cm^{-2}$.[30]

We previously reported that the work function of graphene-covered Ir(111) changes by a small amount with graphene's in-plane orientation.[30] Here we report how the work function changes with a second graphene layer and with the relative orientation of the two layers. We measure work function differences by measuring the energy at which incident electrons begin to be injected into the surface, using the criteria at which 90% of the electrons are reflected.[45] Figure 8 shows that the work functions R22/Ir and R14/Ir are roughly 0.05 eV lower than R0/Ir, similar to the work function lowering of R30/Ir relative to R0/Ir.[30] Thus, the rotated variants consistently have a slightly lower work function than R0/Ir. Figure 8 also demonstrates how the second layer modifies the work function. Figure 8a shows that the work function of R22/R22/Ir is essentially the same as that of R22/Ir. Similarly, Figure 8b shows that the work function of R14/R14/Ir is essentially the same as that of R14/Ir. In other words, the work function does not change with the addition of a second layer of the same orientation. Furthermore, Figure 8a shows that R22/R0/Ir and R0/Ir have essentially the same work functions despite the fact that the R0/Ir and R22/Ir values differ. These observations show that the work function is dominated by the orientation of the graphene layer closest to the Ir. Figure 8b supports this conclusion—R14/R0/Ir and R0/Ir have the same work function. The dominance of the lowest graphene layer is consistent with the interpretation that the work functions of graphene-covered metals arise from effective electric dipoles formed by charge transfer between the substrate and graphene.[46] That is, the charge transfer occurs mainly between the metal and the closest graphene layer.

CONCLUSION

We find that the second graphene layer on Ir(111) nucleates and grows next to the substrate when C is segregating from the substrate or when C is deposited on top of the first graphene layer. This underlayer growth mechanism has significant implications. For example, the nucleation and growth of the second layer strongly depends upon how difficult it is to debond the first layer from the substrate. For a weakly bonded system, such as graphene on Ir, achieving simple layer-by-layer growth is difficult because new layers nucleate before prior layers are completed. On metals that strongly bind graphene, more uniform layer-by-layer growth is possible, as on Ru(0001).[28] Our observation that new layers formed by C deposition grow under existing layers implies that carbon readily intercalates between the first-layer graphene and Ir, even if the defect densities of the graphene films are quite low.[17]

METHODS

Graphene growth was observed in real time by LEEM. For growth by segregation, the Ir(111) crystal at ~1150 °C was loaded with C by exposure to $\sim 1 \times 10^{-8}$ Torr of ethylene. When majority of the surface was covered by single-layer graphene, the ethylene was evacuated and the Ir was cooled over about 1 min to 950−1080 °C. In this temperature range, segregating C completed the first layer and second-layer growth began. C was deposited from exposure to a graphite rod heated by an electron beam. To separate effects of segregation and C deposition, the latter was performed only under the conditions where the rate of segregation was negligible, as determined by monitoring the graphene growth rate prior to C deposition. For some cases, this was achieved by removing some C from the crystal prior to growth using oxygen to burn off graphene.[47,48]

Film thickness (Figure S1b) and work function changes (Figure 8) were measured from the intensity of local regions in a series of LEEM images as a function of incident electron energy. Imaging during growth was performed at electron

energies that gave significant contrast between different layer thicknesses (Figure S1a) and between different in-plane orientations (Figure 2a). Selected-area LEED patterns were obtained using apertures to limit the size of the electron beam on the sample to ~0.5 or ~2 μm in diameter. The analyzed regions consisted of a single film thickness and a single configuration of in-plane orientation of the graphene layers.

The sample characterized by ARPES was a complete first-layer film containing about 20% coverage of second-layer islands, which were about 20 μm in size. After growth and characterization in the LEEM chamber, the sample was transferred in air to the Electronic Structure Factory endstation on beamline 7.0.1 at the Advanced Light Source[6] and annealed at ~500 °C in ultrahigh vacuum to remove adsorbates from the air exposure. The ARPES measurements were conducted with the sample at ~50 K using 130 eV photons with an overall energy resolution of ~25 meV.

Acknowledgment. Work at Sandia was supported by the Office of Basic Energy Sciences, Division of Materials Sciences and Engineering of the U.S. DOE under Contract No. DE-AC04-94AL85000. The Advanced Light Source is supported by the Director, Office of Science, Office of Basic Energy Sciences, of the U.S. Department of Energy under Contract No. DE-AC02-05CH11231.

Supporting Information Available: Figures S1−5 and movies S1−4. This material is available free of charge *via* the Internet at http://pubs.acs.org.

REFERENCES AND NOTES

1. Choi, W.; Lahiri, I.; Seelaboyina, R.; Kang, Y. S. Synthesis of Graphene and Its Applications: A Review. *Crit. Rev. Solid State Mater. Sci.* **2010,** *35*, 52–71.
2. Filleter, T.; McChesney, J. L.; Bostwick, A.; Rotenberg, E.; Emtsev, K. V.; Seyller, T.; Horn, K.; Bennewitz, R. Friction and Dissipation in Epitaxial Graphene Films. *Phys. Rev. Lett.* **2009,** *102*, 086102.
3. Castro Neto, A. H.; Guinea, F.; Peres, N. M. R.; Novoselov, K. S.; Geim, A. K. The Electronic Properties of Graphene. *Rev. Mod. Phys.* **2009,** *81*, 109–162.
4. Schwierz, F. Graphene Transistors. *Nat. Nanotechnol.* **2010,** *5*, 487–496.
5. McCann, E. Asymmetry Gap in the Electronic Band Structure of Bilayer Graphene. *Phys. Rev. B* **2006,** *74*, 161403.
6. Ohta, T.; Bostwick, A.; Seyller, T.; Horn, K.; Rotenberg, E. Controlling the Electronic Structure of Bilayer Graphene. *Science* **2006,** *313*, 951–954.
7. Guinea, F.; Neto, A. H. C.; Peres, N. M. R. Electronic States and Landau Levels in Graphene Stacks. *Phys. Rev. B* **2006,** *73*, 245426.
8. Hass, J.; Varchon, F.; Millan-Otoya, J. E.; Sprinkle, M.; Sharma, N.; De Heer, W. A.; Berger, C.; First, P. N.; Magaud, L.; Conrad, E. H. Why Multilayer Graphene on 4H-SiC-(000−1) Behaves Like a Single Sheet of Graphene. *Phys. Rev. Lett.* **2008,** *100*, 125504.
9. Morgan, A. E.; Somorjai, G. A. Low Energy Electron Diffraction Studies of Gas Adsorption on the Platinum (100) Single Crystal Surface. *Surf. Sci.* **1968,** *12*, 405–425.
10. May, J. W. Platinum Surface LEED Rings. *Surf. Sci.* **1969,** *17*, 267–270.
11. Shelton, J. C.; Patil, H. R.; Blakely, J. M. Equilibrium Segregation of Carbon to a Nickel (111) Surface−Surface Phase-Transition. *Surf. Sci.* **1974,** *43*, 493–520.
12. Hamilton, J. C.; Blakely, J. M. Carbon Segregation to Single Crystal Surfaces of Pt, Pd, and Co. *Surf. Sci.* **1980,** *91*, 199–217.
13. Land, T. A.; Michely, T.; Behm, R. J.; Hemminger, J. C.; Comsa, G. STM Investigation of Single Layer Graphite Structures Produced on Pt(111) by Hydrocarbon Decomposition. *Surf. Sci.* **1992,** *264*, 261–270.
14. N'Diaye, A. T.; Bleikamp, S.; Feibelman, P. J.; Michely, T. Two-Dimensional Ir Cluster Lattice on a Graphene Moiré on Ir(111). *Phys. Rev. Lett.* **2006,** *97*, 215501.
15. Wintterlin, J.; Bocquet, M. L. Graphene on Metal Surfaces. *Surf. Sci.* **2009,** *603*, 1841–1852.
16. Sutter, P. W.; Flege, J.-I.; Sutter, E. A. Epitaxial Graphene on Ruthenium. *Nat. Mater.* **2008,** *7*, 406–411.
17. Coraux, J.; N'Diaye, A. T.; Busse, C.; Michely, T. Structural Coherency of Graphene on Ir(111). *Nano Lett.* **2008,** *8*, 565–570.
18. Loginova, E.; Bartelt, N. C.; Feibelman, P. J.; McCarty, K. F. Evidence for Graphene Growth by C Cluster Attachment. *New J. Phys.* **2008,** *10*, 093026.
19. Loginova, E.; Bartelt, N. C.; Feibelman, P. J.; McCarty, K. F. Factors Influencing Graphene Growth on Metal Surfaces. *New J. Phys.* **2009,** *11*, 063046.
20. McCarty, K. F.; Feibelman, P. J.; Loginova, E.; Bartelt, N. C. Kinetics and Thermodynamics of Carbon Segregation and Graphene Growth on Ru(0001). *Carbon* **2009,** *47*, 1806–1813.
21. Arnoult, W. J.; McLellan, R. B. Solubility of Carbon in Rhodium, Ruthenium, Iridium and Rhenium. *Scripta Metall. Mater.* **1972,** *6*, 1013–1018.
22. Yu, Q. K.; Lian, J.; Siriponglert, S.; Li, H.; Chen, Y. P.; Pei, S. S. Graphene Segregated on Ni Surfaces and Transferred to Insulators. *Appl. Phys. Lett.* **2008,** *93*, 113103.
23. Li, X. S.; Cai, W. W.; An, J. H.; Kim, S.; Nah, J.; Yang, D. X.; Piner, R.; Velamakanni, A.; Jung, I.; Tutuc, E.;*et al.*Large-Area Synthesis of High-Quality and Uniform Graphene Films on Copper Foils. *Science* **2009,** *324*, 1312–1314.
24. Loginova, E.; Nie, S.; Thürmer, K.; Bartelt, N. C.; McCarty, K. F. Defects of Graphene on Ir(111): Rotational Domains and Ridges. *Phys. Rev. B* **2009,** *80*, 085430.
25. Grant, J. T.; Haas, T. W. A Study of Ru(0001) and Rh(111) Surfaces Using LEED and Auger Electron Spectroscopy. *Surf. Sci.* **1970,** *21*, 76–85.
26. Tontegode, A. Y. Carbon on Transition Metal Surfaces. *Prog. Surf. Sci.* **1991,** *38*, 201–429.
27. Gall, N. R.; Rut'Kov, E. V.; Tontegode, A. Y. Two Dimensional Graphite Films on Metals and Their Intercalation. *Int. J. Mod. Phys. B* **1997,** *11*, 1865–1911.
28. Cui, Y.; Fu, Q.; Bao, X. Dynamic Observation of Layer-by-Layer Growth and Removal of Graphene on Ru(0001). *Phys. Chem. Chem. Phys.* **2010,** *12*, 5053–5057.
29. Reina, A.; Jia, X. T.; Ho, J.; Nezich, D.; Son, H. B.; Bulovic, V.; Dresselhaus, M. S.; Kong, J. Large Area, Few-Layer Graphene Films on Arbitrary Substrates by Chemical Vapor Deposition. *Nano Lett.* **2009,** *9*, 30–35.
30. Starodub, E.; Bostwick, A.; Moreschini, L.; Nie, S.; El Gabaly, F.; McCarty, K. F.; Rotenberg, E. In-Plane Orientation Effects on the Electronic Structure, Stability and Raman Scattering of Monolayer Graphene on Ir(111). *Phys. Rev. B* **2010**.
31. Sutter, E.; Albrecht, P.; Sutter, P. Graphene Growth on Polycrystalline Ru Thin Films. *Appl. Phys. Lett.* **2009,** *95*, 133109.
32. We have confirmed this expectation by analyzing LEED from the simpler system of multilayer graphene on Ru-(0001), where all layers have R0-type alignment (see ref 16). Except for small, discrete energy ranges, we find that with increasing energy the first-order Ru spots become increasingly intense relative to the first-order graphene spots for both single-layer and bilayer graphene. Around 200 eV, the first-order Ru spots are generally more intense than the graphene spots.
33. Van Hove, M. A.; Weinberg, W. H.; Chan, C.-M. Low-Energy Electron Diffraction Experiment, Theory and Surface structure Determination; Springer Verlag: Berlin, Heidelberg, 1986; pp 117−120.
34. Nieuwenhuys, B. E.; Hagen, D. I.; Rovida, G.; Somorjai, G. A. LEED, AES and Thermal Desorption Studies of Chemisorbed Hydrogen and Hydrocarbons (C_2H_2,C_2H_4,C_6H_6, C_6H_{12}) on (111) and Stepped 6(111) × (100) Iridium Crystal-Surfaces—Comparison with Platinum. *Surf. Sci.* **1976,** *59*, 155–176.
35. A reason the moiré periodicity is so strong around the R22 features could be that the height corrugations of the R0 moiré cell are imprinted in the overlying R22 layer. Multiple diffraction could also play a role, although strong

sequential diffraction from three layers (R0, R22 and Ir) is needed to explain the rosette features. See: Van Hove, M. A.; Weinberg, W. H.; Chan, C.-M. Low-Energy Electron Diffraction Experiment, Theory and Surface Structure Determination; Springer Verlag: Berlin, Heidelberg, 1986; pp 82−84. The same observations hold for R0/R26/Ir and R26/R0/Ir in Figure 4.

36. We also found examples in growth from segregation where the buried, second layer grew across rotational boundaries in the top layer without altering its orientation with respect to the substrate. Figure S3 provides an example where R0 nucleated under a R30 layer and grew across a rotational boundary.
37. Pimpinelli, A.; Villain, J. Physics of Crystal Growth; Cambridge University Press: Cambridge, 1998; pp 70−87.
38. Other orientations can result from the second layer growing across rotational boundaries in the first layer, however, as shown in Figure 4.
39. Brako, R.; Šokčević, D.; Lazić, P.; Atodiresei, N. Graphene on the Ir(111) Surface: From van der Waals to Strong Bonding. *New J. Phys.* **2010,** *12*, 113016.
40. Chen, H.; Zhu, W. G.; Zhang, Z. Y. Contrasting Behavior of Carbon Nucleation in the Initial Stages of Graphene Epitaxial Growth on Stepped Metal Surfaces. *Phys. Rev. Lett.* **2010,** *104*, 186101.
41. Sutter, P.; Sadowski, J. T.; Sutter, E. Graphene on Pt(111): Growth and Substrate Interaction. *Phys. Rev. B* **2009,** *80*, 245411.
42. Murata, Y.; Starodub, E.; Kappes, B. B.; Ciobanu, C. V.; Bartelt, N. C.; McCarty, K. F.; Kodambaka, S. Unpublished.
43. Mucha-Kruczyński, M.; Tsyplyatyev, O.; Grishin, A.; McCann, E.; Fal'ko, V. I.; Bostwick, A.; Rotenberg, E. Characterization of Graphene through Anisotropy of Constant-Energy Maps in Angle-Resolved Photoemission. *Phys. Rev. B* **2008,** *77*, 195403.
44. Rotational alignment ensures that in reciprocal space the electronic bands are aligned and hence able to interact (see ref 8). In our LEEM analysis, we always find that the second layer under an R0 top sheet also had R0 orientation, a stacking that produces two π-bands. See Figure S1 of Supporting Information.
45. Murata, Y.; Starodub, E.; Kappes, B. B.; Ciobanu, C. V.; Bartelt, N. C.; McCarty, K. F.; Kodambaka, S. Orientation-Dependent Work Function of Graphene on Pd(111). *Appl. Phys. Lett.* **2010,** *97*, 143114.
46. Khomyakov, P. A.; Giovannetti, G.; Rusu, P. C.; Brocks, G.; van den Brink, J.; Kelly, P. J. First-Principles Study of the Interaction and Charge Transfer between Graphene and Metals. *Phys. Rev. B* **2009,** *79*, 195425.
47. van Gastel, R.; N'Diaye, A. T.; Wall, D.; Coraux, J.; Busse, C.; Buckanie, N. M.; zu Heringdorf, F. J. M.; von Hoegen, M. H.; Michely, T.; Poelsema, B. Selecting a Single Orientation for Millimeter Sized Graphene Sheets. *Appl. Phys. Lett.* **2009,** *95*, 121901.
48. Starodub, E.; Bartelt, N. C.; McCarty, K. F. Oxidation of Graphene on Metals. *J. Phys. Chem. C* **2010,** *114*, 5134–5140.